NANO LETTERS

pubs.acs.org/NanoLett

Letter

Inducing Defects in ^{19}F-Nanocrystals Provides Paramagnetic-free Relaxation Enhancement for Improved *In Vivo* Hotspot MRI

Reut Mashiach, Dana Cohen, Liat Avram, Talia Harris, Iddo Pinkas, Lothar Houben, Hyla Allouche-Arnon, and Amnon Bar-Shir*

Cite This: *Nano Lett.* 2020, 20, 7207−7212

Read Online

ACCESS | Metrics & More | Article Recommendations | Supporting Information

ABSTRACT: Paramagnetic relaxation enhancement (PRE) is the current strategy of choice for enhancing magnetic resonance imaging (MRI) contrast and for accelerating MRI acquisition schemes. Yet, debates regarding lanthanides' biocompatibility and PRE-effect on MRI signal quantification have raised the need for alternative strategies for relaxation enhancement. Herein, we show an approach for shortening the spin−lattice relaxation time (T_1) of fluoride-based nanocrystals (NCs) that are used for in vivo ^{19}F-MRI, by inducing crystal defects in their solid-crystal core. By utilizing a phosphate-based rather than a carboxylate-based capping ligand for the synthesis of CaF_2 NCs, we were able to induce grain boundary defects in the NC lattice. The obtained defects led to a 10-fold shorter T_1 of the NCs' fluorides. Such paramagnetic-free relaxation enhancement of CaF_2 NCs, gained without affecting either their size or their colloidal characteristics, improved 4-fold the obtained ^{19}F-MRI signal-to-noise ratio, allowing their use, in vivo, with enhanced hotspot MRI sensitivity.

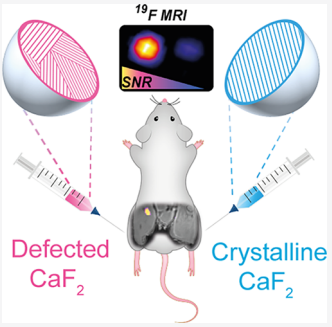

KEYWORDS: *^{19}F-MRI, nanocrystals, crystal engineering, relaxation enhancement, in vivo MRI, crystal defects*

The ability to design and control the physical, chemical, electrical, optical, and magnetic properties of small-sized molecular solids has greatly advanced the field of nanocrystal (NC) engineering[1−4] contributing to the development of nanomedicine.[5] Among their various applications in nanomedicine, NCs are widely used as imaging agents in optical[6] and photoacoustic imaging,[7] computed tomography (CT),[8] and magnetic resonance imaging (MRI),[9] and the ability to engineer them in a desired manner has led to enhanced performance. Crystal engineering has been used, for example, to alter quantum dots' size,[10] shape,[11] and fluorescent properties.[12] Gold NCs have been engineered to have controllable sizes[13] and shapes[14] as a means to enhance their delivery and performance in both CT and photoacoustic imaging.[15] For MRI applications, metal oxide NCs have been designed to have a multimetal core for enhanced sensitivity,[16] manganese-oxide core for positive contrast,[17] micrometer-size for single-cell visualization,[18] or extremely small-size for T_1 contrast enhancement.[19]

Nanosized inorganic fluoride (specifically, CaF_2)[20] NCs have been recently designed and implemented as imaging tracers benefiting from the advantageous background-free ^{19}F-MRI.[21−25] Their small size (<10 nm) and their inorganic solid core make them a unique category of ^{19}F-MRI tracers, distinct from the extensively developed and frequently used perfluorocarbon (PFC) nanoemulsions,[22,23] with the potential to be further developed for applications where small-sized NCs and tunable morphologies are essential.[26,27] However, one of the main limitations of CaF_2 NCs as ^{19}F-MRI agents is their long spin−lattice relaxation time T_1 (>10 s), which prolongs the time of data acquisition when signal averaging is needed for an improved signal-to-noise ratio (SNR). One potential strategy for efficient shortening of the T_1 of the fluorine-19 content is to induce paramagnetic relaxation enhancement (PRE), which was efficiently demonstrated for large-sized PFC nanoemulsions,[28−31] resulting in several-fold enhanced sensitivity of ^{19}F-MRI. Nevertheless, alternatives for paramagnetic dopants need to be considered, not only to address recently raised concerns of lanthanide biocompatibility[32,33] but also to allow robust quantification of the ^{19}F-tracer distribution from the ^{19}F-MR signal, as such quantification has been shown to be far from straightforward in solid-materials in the presence of dopants with a strong PRE effect.[34] Herein, we propose an alternative to the commonly used PRE approach and show that synthetic induction of crystal defects in small-sized CaF_2 NCs significantly shortens the T_1 relaxation time of the fluoride within the NC, allowing improved *in vivo* ^{19}F-MRI sensitivity.

The area of surface chemistry bridges the gap between NCs' fabrication and their properties and has been exploited for strategizing synthetic routes. One approach is to utilize the binding affinities of ligands to the surface of the NCs and their

Received: June 19, 2020
Revised: September 7, 2020
Published: September 8, 2020

precursors in order to manipulate the morphology of nanomaterials.[35] Based on the rationale that Ca^{2+} (a CaF_2 precursor) binds more strongly to phosphate groups than to carboxylate groups,[36] CaF_2 NCs were synthesized with two different ligands, namely, oleic acid (OA, Figure 1a) and oleyl phosphate (OP, Figure 1b). Note that except for their headgroup, OA and OP share identical organic tails, allowing a similar outer coating, essential for their colloidal stability. Indeed, both OA-CaF_2 and OP-CaF_2 fabrications result in a similar small core size (8.3 ± 0.8 nm and 8.0 ± 1.3 nm, respectively, Figure 1a–c) and comparable colloidal diameter (10.5 ± 3.0 nm and 10.4 ± 2.9 nm, respectively, Figure 1d).

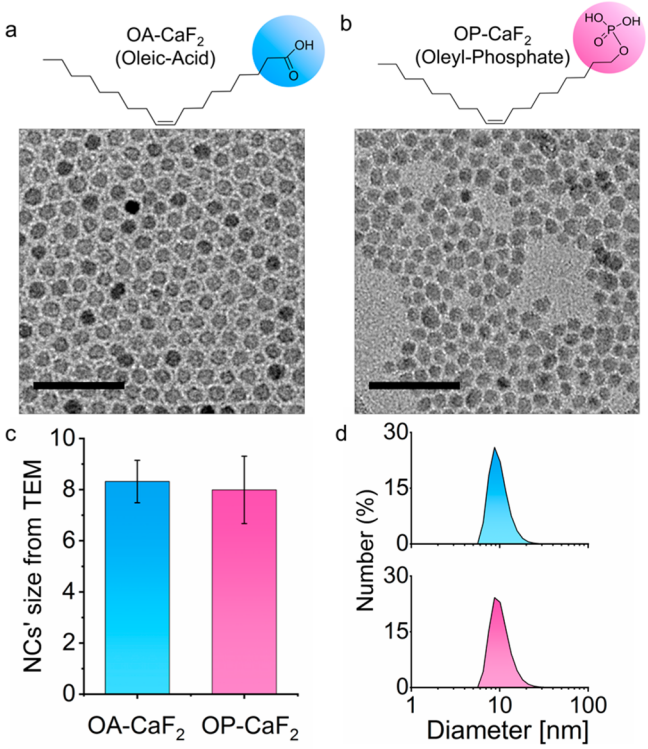

Figure 1. Characterization of OA-CaF_2 and OP-CaF_2 NCs: The molecular structures of the oleic acid (OA, light blue) and the oleyl phosphate (OP, pink) ligands used to synthesize OA-CaF_2 (a) and OP-CaF_2 (b), respectively, and representative TEM images of the NCs (scale bar 50 nm). (c) Average diameter of OA-CaF_2 (8.3 ± 0.8 nm) and OP-CaF_2 NCs (8.0 ± 1.3 nm) as obtained from the TEM images. (d) The colloidal diameter of dispersed OA-CaF_2 (10.5 ± 3.0 nm) and OP-CaF_2 NCs (10.4 ± 2.9 nm) as obtained from DLS measurements.

High-resolution TEM (HR-TEM) analysis of the crystal structure of OP-CaF_2 and OA-CaF_2 at the atomic level revealed a remarkable difference in the crystal architecture of the two types of NCs (Figure 2a and Figure 2b). While OA-CaF_2 NCs exhibited a well-ordered, highly crystalline lattice (Figure 2a), OP-CaF_2 NCs featured clear crystal defects, i.e., grain boundaries (Figure 2b). This observation was further validated by powder X-ray diffraction (XRD) measurements of dried samples of OA-CaF_2 (Figure 2c) and OP-CaF_2 (Figure 2d) NCs, showing wider XRD patterns for the disordered OP-CaF_2 NCs, as demonstrated for other inorganic materials.[37] An additional indication for the polycrystallinity of OP-CaF_2 NCs was obtained using Raman spectroscopy (Figure S1); both line broadening and Raman shifts were observed for OP-CaF_2 NCs

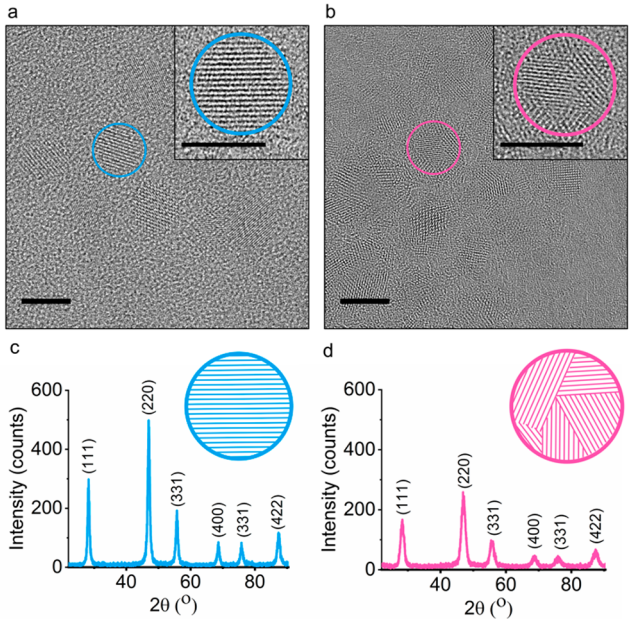

Figure 2. Characterization of OA crystalline features of OA-CaF_2 and OP-CaF_2 NCs. (a, b) HR-TEM image (scale bar 10 nm, in inset 5 nm) of (a) OA-CaF_2 and (b) OP-CaF_2 NCs. (c, d) Powder XRD patterns of dry samples of (c) OA-CaF_2 and (d) OP-CaF_2 NCs.

(as compared to powders of commercial CaF_2 and OA-CaF_2), which can be assigned to a smaller grain size within the polycrystalline material. We attribute the crystallographic differences between OP-CaF_2 and OA-CaF_2 NCs to different growth paths mediated by the nature of the surface ligands present during the synthesis.[38,39]

It was previously shown that crystallographic defects, induced by mechanical stress of large-size CaF_2 crystals, may facilitate element mobility and enhance dipolar interaction, which could induce T_1 shortening[40,41] without the use of paramagnetic elements. Encouraged by these studies and with the vision of using CaF_2 NCs as nanosized tracers for ^{19}F-MRI applications, we studied the effect of their crystal properties on their ^{19}F-NMR characteristics using a liquid-state high-resolution ^{19}F-NMR setup. Notably, both dispersed OA-CaF_2 and OP-CaF_2 NCs produced similar ^{19}F-NMR spectra (Figure S2), with a typical CaF_2 peak at −109 ppm. Interestingly and importantly for their use as nanotracers in ^{19}F-MRI applications, we found a dramatic difference in the T_1 values of the ^{19}F fluoride signal in the colloidal CaF_2 NCs (Figure S3a,b), a result of the pronounced grain boundary defects in OP-CaF_2 NCs (Figure 2b). This 10-fold reduction in T_1 should allow significant improvement in the sensitivity of ^{19}F-MRI studies when using OP-CaF_2 compared to OA-CaF_2 NCs. Note that the short T_2 that is characteristic to nanofluorides was similar in both fabrications (Figure S3c,d); nevertheless, such limitation could be overcome by using an MRI scheme such as ultrashort TE (UTE) or zero TE (ZTE), found to be applicable to both nanofluorides[20] and paramagnetic PFCs.[29]

Next, we assessed whether the significant T_1 relaxation enhancement observed for polycrystalline nanofluorides (OP-CaF_2) as compared to crystalline nanofluorides (OA-CaF_2) in organic solvents could be translatable to improved ^{19}F-MRI sensitivity *in vivo*. For that purpose, both fabrications were transferred from an organic solvent (cyclohexane) to an

https://dx.doi.org/10.1021/acs.nanolett.0c02549
Nano Lett. 2020, 20, 7207−7212

aqueous solution by incorporating phospholipids (PLs) into the hydrophobic tails of their capping ligands and stabilizing these colloids with cholesterol content and polyethylene-glycol-modified phospholipids (Figure 3a and Figure S4). The

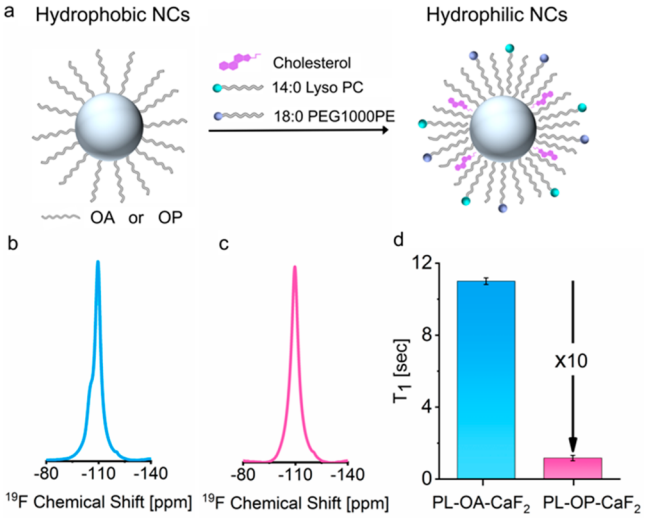

Figure 3. High-resolution ^{19}F-NMR properties of CaF_2 NCs in water. (a) Schematic representation of phase transfer (from organic solvent to water) via ligand incorporation of phospholipids (molecular structures in Figure S4). ^{19}F-NMR spectra of (b) PL-OA-CaF_2 (light-blue) and (c) PL-OP-CaF_2 (pink) dispersed in water. (d) ^{19}F-T_1-relaxation times for PL-OA-CaF_2 (11.0 ± 0.2 s) and PL-OP-CaF_2 NCs (1.2 ± 0.2 s).

resultant colloids endowed both PL-OA-CaF_2 and PL-OP-CaF_2 NCs with water solubility and colloidal stability characteristics suitable for *in vivo* ^{19}F-MRI tracers (Figure S5). The stability of the water dispersed NCs in aqueous media was studied for 40 days by both DLS measurements and high-resolution ^{19}F-NMR spectroscopy (Figure S7), showing their long-term stability and resistance to degradation when stored for future uses. It is important to mention here that the 10-fold difference in the T_1 values of the two types of nanofluorides was preserved for water-dispersed NCs, with 11 ± 0.2 s for PL-OA-CaF_2 and 1 ± 0.2 s for PL-OP-CaF_2 NCs (Figure 3d and Figure S6).

In order to quantify the improvement in ^{19}F-MRI sensitivity upon T_1 shortening, a phantom composed of two tubes with the same ^{19}F concentration, one containing water-dispersed PL-OP-CaF_2 NCs and the other containing water-dispersed PL-OA-CaF_2 NCs, was studied (Figure 4a). Indeed, a four times higher SNR was obtained in ^{19}F-MRI for the tube containing the PL-OP-CaF_2 as compared to that of PL-OA-CaF_2 NCs (Figure 4b,c), acquired with a UTE sequence to detect the ^{19}F-MR signal of the fluorides in the NCs.[20] The 10-fold shorter T_1 of the fluorides in PL-OP-CaF_2 allowed us to shorten dramatically the repetition time (TR) and, thus, to increase the number of signal averages for a given time of acquisition or to shorten the total scan time for a given number of signal averages. Note that in order to obtain a comparable ^{19}F-MRI SNR from the crystalline PL-OA-CaF_2 NCs, a much longer TR was needed, and consequently, a more than 1 h acquisition time to allow the same number of signal averages would be required (compared to the 6.5 min needed for TR = 4.2 ms, Figure 4b,c). In order to obtain a comparable SNR of

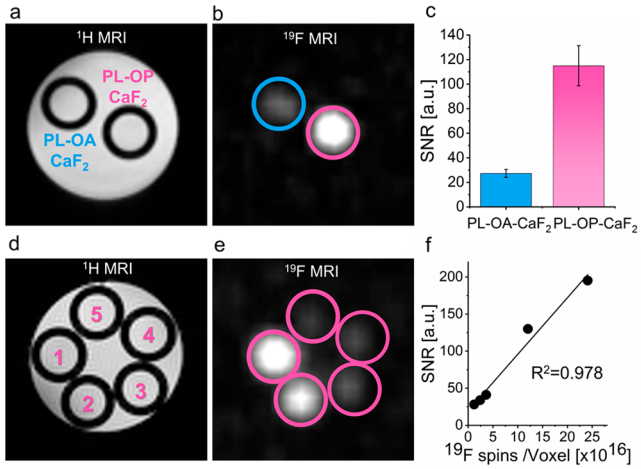

Figure 4. ^{19}F-MRI of CaF_2 NCs. (a) ^{1}H-MRI and (b) ^{19}F-MRI of a phantom composed of two tubes containing either PL-OA-CaF_2 or PL-OP-CaF_2 NCs. For ^{19}F-MRI data, a 3D-UTE sequence was used. (c) Calculated SNR values for of PL-OA-CaF_2 (27 ± 3) and of PL-OP-CaF_2 (115 ± 16) as measured from the ^{19}F-MRI in b. SNR and (d) ^{1}H-MRI and (e) ^{19}F-MRI of a phantom composed of five tubes containing different concentrations of PL-OP-CaF_2 (i.e., total ^{19}F): 100, 50, 15, 10, and 5 mM (1−5, respectively, in d). (f) SNR as a function of ^{19}F atoms per voxel (4 mm^3), as obtained from the data in e.

the two types of NCs using a single-scan acquisition, a ten-time longer acquisition was needed for PL-OA-CaF_2 NCs as compared to that required for PL-OP-CaF_2 NCs (Figure S8).

To quantify the improved sensitivity in ^{19}F-MRI experiments and to examine the detectability level of PL-OP-CaF_2 NCs, a series of tubes containing a range of concentrations was prepared and studied (Figure 4d−f). Notably, by shortening the T_1 values of the nanofluorides by one order of magnitude, we were able to detect low ^{19}F concentrations down to 5 mM, 10 times lower than the detectability level of the highly crystalline CaF_2.[20] For example, an SNR of 28 in the ^{19}F-MRI of the studied phantom was obtained with a 5 mM ^{19}F-concentration (equivalent to 1.2 × 10^{16} fluorine spins) with a voxel size of 4 mm^3, a level of ^{19}F-MRI detectability comparable to that of the commonly used PFC nano-emulsions.[42] The very long T_2 values of PFCs, however, allows us to acquire their ^{19}F-MRI data using multi-echo-based schemes (i.e., RARE or FSE) and thus provide them with essential improved sensitivity for a given time of data acquisition when directly compared to PL-OP-CaF_2 NCs (Figure S9 and Table S1). Nevertheless, it is important to mention that while the short T_2 limitation of PL-OP-CaF_2 could be overcome by using a UTE-MRI scheme, such sequences are still in their infancy. Therefore, we expect that more advanced UTE protocols that allow multi-echo read-outs[43] and those based on compressed sensing[44] should further improve the SNR/time-unit of ^{19}F-MRI data that is based on nanofluorides even at their given short T_2 values.

Moreover, and very importantly, the fact that PL-OP-CaF_2 NCs and PFC-based emulsions differ in size by one order of magnitude (i.e., ∼10 nm for CaF_2 and ∼100 nm for PFCs, Figure S10a) show that each of the nanoformulations could be used and may be more applicable for different approaches due to their expected different biodistribution, clearance profiles, and accessibility to a desired target. Showing that the chemical shift in the ^{19}F-NMR of PFC-based nanoemulsions (−91 ppm

https://dx.doi.org/10.1021/acs.nanolett.0c02549
Nano Lett. 2020, 20, 7207−7212

for VS1000) differs from that of CaF_2 NCs (−109 ppm) by almost 20 ppm demonstrates the potential of using the two nanofabrications in future "multicolor" ^{19}F-MRI studies (Figure S10b−h). Thus, capitalizing on this multiplexing feature, given their very different hydrodynamic diameter (Figure S10a), may open new opportunities to combine these nanoformulations for noninvasive multiplexed imaging, for example, in studies where the size of the imaging agent is essential.

Finally, to evaluate the potential of PL-OP-CaF_2 NCs as imaging tracers for in vivo ^{19}F-MRI applications and to determine the gain in sensitivity, noninvasively, in a live intact subject, both designed NCs were intramuscularly injected into mouse legs (Figure 5a) after determining their cytotoxicity

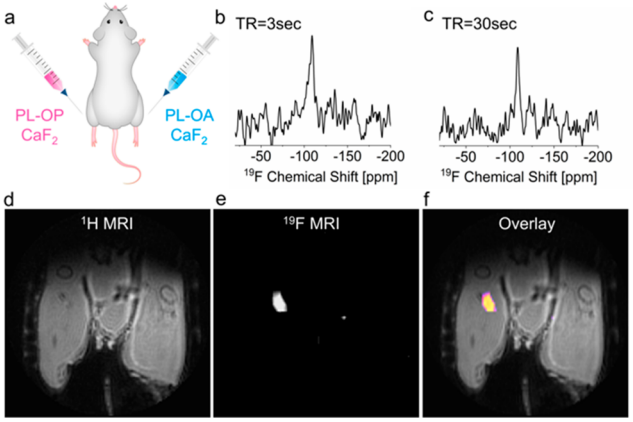

Figure 5. In vivo ^{19}F-NMR and ^{19}F-MRI of injected PL-OA-CaF_2 and PL-OP-CaF_2 NCs. (a) Scheme of the injection setup. (b) ^{19}F-ISIS spectra acquired from the right leg (PL-OP- CaF_2 injection) using TR = 3 s and (c) from the left leg (PL-OA-CaF_2 injection) using TR = 30 s. (d) ^{1}H-MRI, (e) ^{19}F-MRI (acquired with a 3D-UTE sequence), and (f) ^{19}F-MRI shown as a pseudocolor map overlaid on the anatomical ^{1}H-MR image of a live mouse.

profile using three different cell-based assays, namely, (*i*) CCK-8 assay (Figure S11), (*ii*) MTT assay (Figure S12), and (*iii*) LDH-cytotoxicity assay (Figure S13). A localized ^{19}F-NMR spectrum of each leg showed a comparable intensity of the CaF_2 peak (−109 ppm; Figure 5b,c and Figure S14) when the acquisition parameters were adjusted to the T_1 properties of each formulation, indicating the comparable CaF_2 concentration in the two injection sites. Significantly, although the same fluoride content was confirmed for both injections, a notable ^{19}F-MRI signal was picked up only in the leg injected with PL-OP-CaF_2 NCs (Figure 5d,e), which could be displayed as a "hotspot" map overlaid on anatomical high-resolution ^{1}H-MRI (Figure 5f). These results demonstrate that, while avoiding the use of paramagnetic elements and without introducing the PRE-effect for shortening T_1 values, we were able to extensively enhance the longitudinal relaxation rates of small-sized fluoride-NCs to improve ^{19}F-MRI performances.

In summary, we propose here a paramagnetic-free approach for T_1-relaxation enhancement as an alternative to the extensively used PRE effect, avoiding the need for paramagnetic elements in MRI studies. We demonstrate that inducing defects in small-sized nanofluorides allows us to shorten the T_1 of their fluoride content by 10-fold, resulting in a 4-fold increase in the SNR of ^{19}F-MRI studies at a given scan time. While PRE has been at the core of many MRI studies for many decades,[45] allowing researchers to shorten both transverse[46] and longitudinal[47] relaxation times for enhanced image contrast, it has been exploited also to shorten the T_1 values of fluorinated materials[29] for improved SNR in ^{19}F-MRI studies. Our demonstration that controlling the synthetic conditions of fluoride-based NCs and engineering crystal defects (specifically, grain boundaries) to shorten the T_1 of nanofluorides, which together with their manifested in vivo capabilities, offers a novel strategy for fabricating paramagnetic-free nanotracers for in vivo ^{19}F MRI studies. While there is still a scope for shortening the T_1 of nanoflurides, the presented approach for nanocrystalline-defects relaxation enhancement (NDRE) should be further developed by using other strategies to rationalize architecture-relaxation relationships in NCs that are proposed as imaging nanotracers for "hotspot" MRI, even beyond nanofluorides.

■ ASSOCIATED CONTENT

Supporting Information

The Supporting Information is available free of charge at https://pubs.acs.org/doi/10.1021/acs.nanolett.0c02549.

Experimental methods and supplementary figures (PDF)

■ AUTHOR INFORMATION

Corresponding Author

Amnon Bar-Shir − *Department of Organic Chemistry, Weizmann Institute of Science, Rehovot 7610001, Israel;* orcid.org/0000-0003-1431-0221; Email: amnon.barshir@weizmann.ac.il

Authors

Reut Mashiach − *Department of Organic Chemistry, Weizmann Institute of Science, Rehovot 7610001, Israel*

Dana Cohen − *Department of Organic Chemistry, Weizmann Institute of Science, Rehovot 7610001, Israel*

Liat Avram − *Department of Chemical Research Support, Weizmann Institute of Science, Rehovot 7610001, Israel;* orcid.org/0000-0001-6535-3470

Talia Harris − *Department of Chemical Research Support, Weizmann Institute of Science, Rehovot 7610001, Israel*

Iddo Pinkas − *Department of Chemical Research Support, Weizmann Institute of Science, Rehovot 7610001, Israel;* orcid.org/0000-0001-7434-9844

Lothar Houben − *Department of Chemical Research Support, Weizmann Institute of Science, Rehovot 7610001, Israel;* orcid.org/0000-0003-0200-3611

Hyla Allouche-Arnon − *Department of Organic Chemistry, Weizmann Institute of Science, Rehovot 7610001, Israel*

Complete contact information is available at: https://pubs.acs.org/10.1021/acs.nanolett.0c02549

Notes

The authors declare no competing financial interest.

■ ACKNOWLEDGMENTS

This project has received funding from the European Research Council (ERC) under the European Union's Horizon 2020 research and innovation programme (grant agreement no. 677715).

https://dx.doi.org/10.1021/acs.nanolett.0c02549
Nano Lett. 2020, 20, 7207−7212

REFERENCES

(1) Talapin, D. V.; Lee, J. S.; Kovalenko, M. V.; Shevchenko, E. V. Prospects of colloidal nanocrystals for electronic and optoelectronic applications. *Chem. Rev.* **2010**, *110* (1), 389−458.

(2) Yin, Y.; Alivisatos, A. P. Colloidal nanocrystal synthesis and the organic-inorganic interface. *Nature* **2005**, *437* (7059), 664−70.

(3) De Trizio, L.; Manna, L. Forging Colloidal Nanostructures via Cation Exchange Reactions. *Chem. Rev.* **2016**, *116* (18), 10852−87.

(4) Heuer-Jungemann, A.; Feliu, N.; Bakaimi, I.; Hamaly, M.; Alkilany, A.; Chakraborty, I.; Masood, A.; Casula, M. F.; Kostopoulou, A.; Oh, E.; Susumu, K.; Stewart, M. H.; Medintz, I. L.; Stratakis, E.; Parak, W. J.; Kanaras, A. G. The Role of Ligands in the Chemical Synthesis and Applications of Inorganic Nanoparticles. *Chem. Rev.* **2019**, *119* (8), 4819−4880.

(5) Blanco, E.; Shen, H.; Ferrari, M. Principles of nanoparticle design for overcoming biological barriers to drug delivery. *Nat. Biotechnol.* **2015**, *33* (9), 941−51.

(6) Michalet, X.; Pinaud, F. F.; Bentolila, L. A.; Tsay, J. M.; Doose, S.; Li, J. J.; Sundaresan, G.; Wu, A. M.; Gambhir, S. S.; Weiss, S. Quantum dots for live cells, in vivo imaging, and diagnostics. *Science* **2005**, *307* (5709), 538−44.

(7) Tirotta, I.; Dichiarante, V.; Pigliacelli, C.; Cavallo, G.; Terraneo, G.; Bombelli, F. B.; Metrangolo, P.; Resnati, G. 19F Magnetic Resonance Imaging (MRI): From Design of Materials to Clinical Applications. *Chem. Rev.* **2015**, *115* (2), 1106−1129.

(8) Popovtzer, R.; Agrawal, A.; Kotov, N. A.; Popovtzer, A.; Balter, J.; Carey, T. E.; Kopelman, R. Targeted gold nanoparticles enable molecular CT imaging of cancer. *Nano Lett.* **2008**, *8* (12), 4593−6.

(9) Huh, Y. M.; Jun, Y. W.; Song, H. T.; Kim, S.; Choi, J. S.; Lee, J. H.; Yoon, S.; Kim, K. S.; Shin, J. S.; Suh, J. S.; Cheon, J. In vivo magnetic resonance detection of cancer by using multifunctional magnetic nanocrystals. *J. Am. Chem. Soc.* **2005**, *127* (35), 12387−91.

(10) Cademartiri, L.; Montanari, E.; Calestani, G.; Migliori, A.; Guagliardi, A.; Ozin, G. A. Size-dependent extinction coefficients of PbS quantum dots. *J. Am. Chem. Soc.* **2006**, *128* (31), 10337−46.

(11) Peng, X.; Manna, L.; Yang, W.; Wickham, J.; Scher, E.; Kadavanich, A.; Alivisatos, A. P. Shape control of CdSe nanocrystals. *Nature* **2000**, *404* (6773), 59−61.

(12) Xiong, H. M.; Shchukin, D. G.; Mohwald, H.; Xu, Y.; Xia, Y. Y. Sonochemical synthesis of highly luminescent zinc oxide nanoparticles doped with magnesium(II). *Angew. Chem., Int. Ed.* **2009**, *48* (15), 2727−31.

(13) Chhour, P.; Kim, J.; Benardo, B.; Tovar, A.; Mian, S.; Litt, H. I.; Ferrari, V. A.; Cormode, D. P. Effect of Gold Nanoparticle Size and Coating on Labeling Monocytes for CT Tracking. *Bioconjugate Chem.* **2017**, *28* (1), 260−269.

(14) Huang, P.; Bao, L.; Zhang, C.; Lin, J.; Luo, T.; Yang, D.; He, M.; Li, Z.; Gao, G.; Gao, B.; Fu, S.; Cui, D. Folic acid-conjugated silica-modified gold nanorods for X-ray/CT imaging-guided dual-mode radiation and photo-thermal therapy. *Biomaterials* **2011**, *32* (36), 9796−809.

(15) Chen, Y. S.; Zhao, Y.; Yoon, S. J.; Gambhir, S. S.; Emelianov, S. Miniature gold nanorods for photoacoustic molecular imaging in the second near-infrared optical window. *Nat. Nanotechnol.* **2019**, *14* (5), 465−472.

(16) Lee, J. H.; Huh, Y. M.; Jun, Y. W.; Seo, J. W.; Jang, J. T.; Song, H. T.; Kim, S.; Cho, E. J.; Yoon, H. G.; Suh, J. S.; Cheon, J. Artificially engineered magnetic nanoparticles for ultra-sensitive molecular imaging. *Nat. Med.* **2007**, *13* (1), 95−9.

(17) Kim, T.; Momin, E.; Choi, J.; Yuan, K.; Zaidi, H.; Kim, J.; Park, M.; Lee, N.; McMahon, M. T.; Quinones-Hinojosa, A.; Bulte, J. W.; Hyeon, T.; Gilad, A. A. Mesoporous silica-coated hollow manganese oxide nanoparticles as positive T1 contrast agents for labeling and MRI tracking of adipose-derived mesenchymal stem cells. *J. Am. Chem. Soc.* **2011**, *133* (9), 2955−61.

(18) Shapiro, E. M.; Skrtic, S.; Sharer, K.; Hill, J. M.; Dunbar, C. E.; Koretsky, A. P. MRI detection of single particles for cellular imaging. *Proc. Natl. Acad. Sci. U. S. A.* **2004**, *101* (30), 10901−6.

(19) Kim, B. H.; Lee, N.; Kim, H.; An, K.; Park, Y. I.; Choi, Y.; Shin, K.; Lee, Y.; Kwon, S. G.; Na, H. B.; Park, J. G.; Ahn, T. Y.; Kim, Y. W.; Moon, W. K.; Choi, S. H.; Hyeon, T. Large-scale synthesis of uniform and extremely small-sized iron oxide nanoparticles for high-resolution T1 magnetic resonance imaging contrast agents. *J. Am. Chem. Soc.* **2011**, *133* (32), 12624−31.

(20) Ashur, I.; Allouche-Arnon, H.; Bar-Shir, A. Calcium Fluoride Nanocrystals: Tracers for In Vivo 19F Magnetic Resonance Imaging. *Angew. Chem., Int. Ed.* **2018**, *57* (25), 7478−7482.

(21) Ahrens, E. T.; Flores, R.; Xu, H.; Morel, P. A. In vivo imaging platform for tracking immunotherapeutic cells. *Nat. Biotechnol.* **2005**, *23* (8), 983−7.

(22) Flogel, U.; Ding, Z.; Hardung, H.; Jander, S.; Reichmann, G.; Jacoby, C.; Schubert, R.; Schrader, J. In vivo monitoring of inflammation after cardiac and cerebral ischemia by fluorine magnetic resonance imaging. *Circulation* **2008**, *118* (2), 140−8.

(23) Tirotta, I.; Mastropietro, A.; Cordiglieri, C.; Gazzera, L.; Baggi, F.; Baselli, G.; Bruzzone, M. G.; Zucca, I.; Cavallo, G.; Terraneo, G.; Baldelli Bombelli, F.; Metrangolo, P.; Resnati, G. A superfluorinated molecular probe for highly sensitive in vivo(19)F-MRI. *J. Am. Chem. Soc.* **2014**, *136* (24), 8524−7.

(24) Thurecht, K. J.; Blakey, I.; Peng, H.; Squires, O.; Hsu, S.; Alexander, C.; Whittaker, A. K. Functional hyperbranched polymers: toward targeted in vivo 19F magnetic resonance imaging using designed macromolecules. *J. Am. Chem. Soc.* **2010**, *132* (15), 5336−7.

(25) Nakamura, T.; Sugihara, F.; Matsushita, H.; Yoshioka, Y.; Mizukami, S.; Kikuchi, K. Mesoporous silica nanoparticles for (19)F magnetic resonance imaging, fluorescence imaging, and drug delivery. *Chem. Sci.* **2015**, *6* (3), 1986−1990.

(26) Cabral, H.; Matsumoto, Y.; Mizuno, K.; Chen, Q.; Murakami, M.; Kimura, M.; Terada, Y.; Kano, M. R.; Miyazono, K.; Uesaka, M.; Nishiyama, N.; Kataoka, K. Accumulation of sub-100 nm polymeric micelles in poorly permeable tumours depends on size. *Nat. Nanotechnol.* **2011**, *6* (12), 815−23.

(27) Betzer, O.; Shilo, M.; Opochinsky, R.; Barnoy, E.; Motiei, M.; Okun, E.; Yadid, G.; Popovtzer, R. The effect of nanoparticle size on the ability to cross the blood-brain barrier: an in vivo study. *Nanomedicine* **2017**, *12* (13), 1533−1546.

(28) de Vries, A.; Moonen, R.; Yildirim, M.; Langereis, S.; Lamerichs, R.; Pikkemaat, J. A.; Baroni, S.; Terreno, E.; Nicolay, K.; Strijkers, G. J.; Grull, H. Relaxometric studies of gadolinium-functionalized perfluorocarbon nanoparticles for MR imaging. *Contrast Media Mol. Imaging* **2014**, *9* (1), 83−91.

(29) Kislukhin, A. A.; Xu, H.; Adams, S. R.; Narsinh, K. H.; Tsien, R. Y.; Ahrens, E. T. Paramagnetic fluorinated nanoemulsions for sensitive cellular fluorine-19 magnetic resonance imaging. *Nat. Mater.* **2016**, *15* (6), 662−8.

(30) Jahromi, A. H.; Wang, C.; Adams, S. R.; Zhu, W.; Narsinh, K.; Xu, H.; Gray, D. L.; Tsien, R. Y.; Ahrens, E. T. Fluorous-Soluble Metal Chelate for Sensitive Fluorine-19 Magnetic Resonance Imaging Nanoemulsion Probes. *ACS Nano* **2019**, *13* (1), 143−151.

(31) Peng, Q.; Li, Y.; Bo, S.; Yuan, Y.; Yang, Z.; Chen, S.; Zhou, X.; Jiang, Z. X. Paramagnetic nanoemulsions with unified signals for sensitive (19)F MRI cell tracking. *Chem. Commun.* **2018**, *54* (47), 6000−6003.

(32) Rogosnitzky, M.; Branch, S. Gadolinium-based contrast agent toxicity: a review of known and proposed mechanisms. *BioMetals* **2016**, *29* (3), 365−76.

(33) Gale, E. M.; Atanasova, I. P.; Blasi, F.; Ay, I.; Caravan, P. A Manganese Alternative to Gadolinium for MRI Contrast. *J. Am. Chem. Soc.* **2015**, *137* (49), 15548−57.

(34) Li, W.; Zhang, Q.; Joos, J. J.; Smet, P. F.; Schmedt auf der Günne, J. Blind spheres of paramagnetic dopants in solid state NMR. *Phys. Chem. Chem. Phys.* **2019**, *21* (19), 10185−10194.

(35) Yang, Z.; Dobbie, A. R.; Cui, K.; Veinot, J. G. A convenient method for preparing alkyl-functionalized silicon nanocubes. *J. Am. Chem. Soc.* **2012**, *134* (34), 13958−61.

https://dx.doi.org/10.1021/acs.nanolett.0c02549
Nano Lett. 2020, 20, 7207−7212

(36) Gebauer, D.; Cölfen, H.; Verch, A.; Antonietti, M. The Multiple Roles of Additives in CaCO3 Crystallization: A Quantitative Case Study. *Adv. Mater.* **2009**, *21* (4), 435−439.
(37) Abdellatief, M.; Abele, M.; Leoni, M.; Scardi, P. Solid State Nuclear Magnetic Resonance and X-ray Diffraction Line Profile Analysis of heavily deformed fluorite. *Thin Solid Films* **2013**, *530*, 44−48.
(38) Pan, A.; He, B.; Fan, X.; Liu, Z.; Urban, J. J.; Alivisatos, A. P.; He, L.; Liu, Y. Insight into the Ligand-Mediated Synthesis of Colloidal CsPbBr3 Perovskite Nanocrystals: The Role of Organic Acid, Base, and Cesium Precursors. *ACS Nano* **2016**, *10* (8), 7943−54.
(39) Sun, S.; Yuan, D.; Xu, Y.; Wang, A.; Deng, Z. Ligand-Mediated Synthesis of Shape-Controlled Cesium Lead Halide Perovskite Nanocrystals via Reprecipitation Process at Room Temperature. *ACS Nano* **2016**, *10* (3), 3648−57.
(40) Heitjans, P.; Indris, S. J. J. o. m. s. Fast diffusion in nanocrystalline ceramics prepared by ball milling. *J. Mater. Sci.* **2004**, *39* (16−17), 5091−5096.
(41) Ruprecht, B.; Wilkening, M.; Steuernagel, S.; Heitjans, P. J. J. o. m. c. Anion diffusivity in highly conductive nanocrystalline BaF_2:CaF_2 composites prepared by high-energy ball milling. *J. Mater. Chem.* **2008**, *18* (44), 5412−5416.
(42) Waiczies, S.; Millward, J. M.; Starke, L.; Delgado, P. R.; Huelnhagen, T.; Prinz, C.; Marek, D.; Wecker, D.; Wissmann, R.; Koch, S. P.; Boehm-Sturm, P.; Waiczies, H.; Niendorf, T.; Pohlmann, A. Enhanced Fluorine-19 MRI Sensitivity using a Cryogenic Radiofrequency Probe: Technical Developments and Ex Vivo Demonstration in a Mouse Model of Neuroinflammation. *Sci. Rep.* **2017**, *7* (1), 9808.
(43) Niedbalski, P. J.; Cochran, A. S.; Akinyi, T. G.; Thomen, R. P.; Fugate, E. M.; Lindquist, D. M.; Pratt, R. G.; Cleveland, Z. I. Preclinical hyperpolarized (129) Xe MRI: ventilation and T2 * mapping in mouse lungs at 7 T using multi-echo flyback UTE. *NMR Biomed.* **2020**, *33* (7), No. e4302.
(44) Fabich, H. T.; Benning, M.; Sederman, A. J.; Holland, D. J. Ultrashort echo time (UTE) imaging using gradient pre-equalization and compressed sensing. *J. Magn. Reson.* **2014**, *245*, 116−24.
(45) Lauffer, R. B. Paramagnetic metal complexes as water proton relaxation agents for NMR imaging: theory and design. *Chem. Rev.* **1987**, *87* (5), 901−927.
(46) Na, H. B.; Song, I. C.; Hyeon, T. Inorganic Nanoparticles for MRI Contrast Agents. *Adv. Mater.* **2009**, *21* (21), 2133−2148.
(47) Caravan, P.; Ellison, J. J.; McMurry, T. J.; Lauffer, R. B. Gadolinium(III) Chelates as MRI Contrast Agents: Structure, Dynamics, and Applications. *Chem. Rev.* **1999**, *99* (9), 2293−2352.

https://dx.doi.org/10.1021/acs.nanolett.0c02549
Nano Lett. 2020, 20, 7207−7212